Applied Catalysis B: Environment and Energy 346 (2024) 123721

Contents lists available at ScienceDirect

Applied Catalysis B: Environment and Energy

journal homepage: www.elsevier.com/locate/apcatb

# Carbon dots bridged $Zn_{0.5}Cd_{0.5}S$ with interfacial amide bond facilitating electron transfer for efficient photocatalytic hydrogen peroxide production

Ting Tang [a,b,1], Jiwu Zhao [c,1], Yongli Shen [b], Fan Yang [a,*], Shuang Yao [b], Changhua An [a,b,**]

[a] Tianjin Key Laboratory of Organic Solar Cells and Photochemical Conversion, School of Chemistry and Chemical Engineering, Tianjin University of Technology, Tianjin 300384, China

[b] Tianjin Key Laboratory of Advanced Functional Porous Materials, Institute for New Energy Materials & Low-Carbon Technologies, School of Materials Science and Engineering, Tianjin University of Technology, Tianjin 300384, China

[c] State Key Laboratory of Photocatalysis on Energy and Environment, College of Chemistry, Fuzhou University, Fuzhou 350116, Fujian, China

ARTICLE INFO

*Keywords:*
Photocatalysis
Hydrogen peroxide
$Zn_{0.5}Cd_{0.5}S$
Carbon dots

ABSTRACT

Photocatalytic $H_2O_2$ production has gained significant attention as an environmentally friendly approach. The key is to explore efficient photocatalysts with sufficient active sites and excellent electron transfer capacity. Herein, we propose a novel approach by incorporating carbon dots (CDs) on ethylenediamine capped $Zn_{0.5}Cd_{0.5}S$, which was bridged with an interfacial amide bond. Smooth transfer of photoinduced electrons from $Zn_{0.5}Cd_{0.5}S$ to carbon dots via a high-speed electron channel is afforded by interfacial amide bond. A remarkable $H_2O_2$ yield with a rate of 252 μmol/h and an apparent quantum yield (AQY) of 31 % at 400 nm is achieved. Photoelectrochemical analysis and density function theory (DFT) calculation reveal CDs with abundant oxygenous functional groups as active sites, boosting activity and selectivity. This interfacial engineering strategy with the acceleration of electrons transfer and enhanced $2e^-$ selectivity can be applied to advanced photocatalytic systems for the achievement of valuable organics, environmental purification and new energy carriers.

## 1. Introduction

Hydrogen peroxide ($H_2O_2$) is an essential chemical and energy storage carrier, which has been widely applied in water remediation, paper bleaching and other fields [1–5]. More than 95 % of commercial $H_2O_2$ is produced through the traditional anthraquinone method. However, the anthraquinone oxidation method relies on the use of noble metals and liquid-liquid extraction, resulting in serious environmental issue and energy consumption. Thus, there is an urgent need to develop a green and energy-efficient approach for $H_2O_2$ production [6–10]. Photocatalytic $2e^-$ $O_2$ reduction is regarded as a promising and sustainable alternative for $H_2O_2$ production because of the energy-saving and environmental benign characteristics [11–15]. Photocatalyst is the key determining the reaction efficiency. Various semiconductor photocatalysts including $TiO_2$, ZnO, graphitic carbon nitrides (g-$C_3N_4$), and organic polymers have been explored for $H_2O_2$ photosynthesis [16–18]. Nevertheless, the limited ability to harvest visible light hinders the effective utilization of solar light utilization. $Zn_xCd_{1-x}S$ solid solution with good visible absorption and tunable band gap exhibits attractive photocatalytic performance in water splitting, $CO_2$ reduction, and $N_2$ reduction [19–21]. However, the lack of sufficient active sites for $O_2$ adsorption and reduction, along with severe recombination of photogenerated charges poses challenges for the application of $Zn_xCd_{1-x}S$ in photocatalytic $O_2$ reduction reaction (ORR).

Carbon dots (CDs) is a class of 0-dimensional (0D) nanomaterials with a diameter of less than 10 nm and abundant oxygenous functional groups (–COOH, –OH, –C═O, etc.) [22,23]. These functional groups confer CDs with good water solubility and allow for their integration with other materials. Notably, high oxygen-doping CDs have recently demonstrated efficient electrocatalytic $H_2O_2$ evolution [24]. Due to their rich $O_2$ activation sites and suitable band structure, CDs serve as excellent cocatalysts, promoting oxygen activation and enhancing selectivity towards $H_2O_2$. Furthermore, the prompt transfer of electrons from $Zn_xCd_{1-x}S$ to CDs effectively suppresses the recombination of

* Corresponding author.
** Corresponding author at: Tianjin Key Laboratory of Organic Solar Cells and Photochemical Conversion, School of Chemistry and Chemical Engineering, Tianjin University of Technology, Tianjin 300384, China.
*E-mail addresses:* fanyang@email.tjut.edu.cn (F. Yang), anch@tjut.edu.cn (C. An).
[1] These authors contributed equally to this work.

https://doi.org/10.1016/j.apcatb.2024.123721
Received 18 November 2023; Received in revised form 4 January 2024; Accepted 8 January 2024
Available online 10 January 2024

photoinduced carriers. Therefore, the incorporation of CDs as co-catalysts for the ORR on $Zn_xCd_{1-x}S$ is a promising strategy for enhancing the activity and selectivity in $H_2O_2$ production.

Herein, CDs decorated $Zn_{0.5}Cd_{0.5}S$ bridging with interfacial amide bond between CDs with carboxyl group and ethylenediamine adsorbed on the surface of $Zn_{0.5}Cd_{0.5}S$ was fabricated through one-pot hydrothermal reaction. The formation of interfacial amide bond facilitates the transfer of photoinduced electron from $Zn_{0.5}Cd_{0.5}S$ to CDs. Moreover, the presence of CDs with abundant oxygenous groups promotes $O_2$ activation and enhances the selectivity of $2e^-$ ORR. Consequently, an impressive $H_2O_2$ photogeneration rate of 252 μmol/h and an apparent quantum yield (AQY) of 31 % at 400 nm has been achieved over the optimized catalyst. This work provides novel insights and a design strategy for highly efficient photocatalytic ORR system.

## 2. Experimental section

### 2.1. Synthesis of CDs

CDs was prepared by an electrochemical method [25]. The electrolyte was prepared by dissolving 1.0 g of NaOH in a mixed solution containing 140 mL of absolute ethanol and 10 mL of deionized water. Two pieces of platinum foils (1.5 cm × 1.5 cm) were used as the anode and counter electrode, respectively. The entire synthesis process was conducted under a direct-current power with a static potential of 20 V. After a reaction time of 24 h, a dark brown solution was obtained and the solvent was subsequently removed via rotary evaporation. The resulting solid was then dissolved in deionized water and purified using dialysis. The concentration of the resulting CDs solution was determined to be 1.3 mg/mL.

### 2.2. Synthesis of CDs decorated $Zn_{0.5}Cd_{0.5}S$

In a typical procedure [26], 0.5 mmol of $Zn(NO_3)_2{\cdot}6\ H_2O$ and 0.5 mmol of $Cd(NO_3)_2{\cdot}4\ H_2O$ were dissolved in (10-X) mL of deionized water. Then, X mL of ethylenediamine (EDA) and 10 mL of CDs solution were added under stirring. A specific concentration of thiourea (Tu) solution (5 mL) was added to the above solution and stirred for 4 h. The obtained mixture was transferred to Teflon-lined autoclave (50 mL) and kept at 200 ℃ for 12 h. The product was collected through centrifugation, and washed thoroughly with deionized water. The as-prepared samples were named as $ZCS_{XEDA\text{-}10CDs}$ (X = 0.3, 1, 3, 5), in which X represents the volume of ethylenediamine used in the reaction.

### 2.3. Synthesis of control samples

To investigate the key factors contributing to the improved performance, several reference samples were prepared, including $ZCS_{1EDA}$, $ZCS_{10CDs}$, $ZCS_{H2O}$, CDs/$ZCS_{1EDA}$, and CDs-EDA. $ZCS_{1EDA}$, $ZCS_{10CDs}$, and $ZCS_{H2O}$ were synthesized without CDs, ethylenediamine, CDs and ethylenediamine, respectively. CDs/$ZCS_{1EDA}$ was prepared through the adsorption treatment of $ZCS_{1EDA}$ (0.1 g) in 10 mL of CDs solution under 25 ℃ for 12 h. CDs-EDA was synthesized through the hydrothermal reaction of CDs solution (10 mL) and ethylenediamine (1 mL) under 200 ℃ for 12 h. The residual ethylenediamine was removed through dialysis.

### 2.4. Characterizations

X-ray diffraction (XRD) patterns were obtained using a Rigaku Corporation UltimaIV diffractometer with a Cu Kα radiation source (λ = 0.15418 nm). The microstructure of products was observed by scanning electronic microscope (SEM, ZEISS MERLIN Compact, Germany), transmission electron microscope (TEM, Tecnai G2 Spirit TWIN, FEI), and high-resolution transmission electron microscope (HRTEM) with FEG (Talos F200 X). The surface composition and valence state were investigated by X-ray photoelectron spectroscopy (XPS, ESCALAB 250Xi). The light absorption property was studied using a UV-2700 spectrophotometer (Shimadzu). The steady photoluminescence (PL) data and transient PL decay spectra were measured on a FL3–2-IHR221-NIR-TCSPC fluorescence spectrometer and Micro Time 200 spectrometer, respectively. The detection of superoxide radical intermediate was carried out on an electron paramagnetic resonance (EPR) spectrometer (EMXplus-6/1, Germany).

### 2.5. Evaluation of photocatalytic $H_2O_2$ production performance

Photocatalytic $H_2O_2$ production was evaluated according to our previous work [27]. Typically, catalyst (50 mg) was dispersed in 50 mL of ethanol/water solution (10 vol%) by ultrasonication. The resulting dispersion was then transferred to a quartz reaction vessel with a volume of 100 mL and $O_2$ was bubbled through the solution under stirring for 30 min. The dispersion was then irradiated with visible light acquired by a 300 W Xe lamp (CEL-HXF300/300 UV) with a UVCUT 400 filter. The reaction temperature was maintained with a water recycle system. A certain amount of dispersion was sampled and filtered using a 0.22 μm needle filter. To the filtrate (1 mL), 1 mL of $CuSO_4$ (0.01 M), 1 mL of buffer solution (pH = 6.86) and 1 mL of 2, 9-dimethyl-1,10-phenanthroline (DMP, 10 g/L) were added. Finally, deionized water was added to kept a constant volume of 10 mL. The concentration of $H_2O_2$ was analyzed using a spectrophotometric method with a UV–vis spectrophotometer and calculated according to the calibration curve (Fig. S1).

### 2.6. Calculation of apparent quantum yield (AQY)

The calculation of AQY was conducted by measuring the photocatalytic performance under the irradiation of monochromatic light, which was acquired from a 300 W Xe lamp equipped with a band-pass filter. The average light intensity was obtained through a CELNP2000 optical power meter. The amount of produced $H_2O_2$ was determined by the spectrophotometric method described above. AQY was calculated according to the following equation:

$$AQY = N\ (H_2O_2) \times 2 / N\ (Photons) \times 100\ \%$$

N ($H_2O_2$) and N (Photons) represent the mole number of generated $H_2O_2$ and incident photons in 1 h, respectively.

### 2.7. Electrochemical and photoelectrochemical tests

Rotating disk electrode (RDE) measurement was carried out on an electrochemical workstation (Chenhua CHI 760E) with a conventional three-electrode system. An Ag/AgCl electrode, a platinum wire, and a glassy carbon electrode coated with photocatalysts were utilized as the reference electrode, counter electrode and working electrode respectively. To fabricate the working electrode, 5 mg of the sample was dispersed to a mixed solution consisting of 50 μL of Nafion solution and 0.45 mL of ethanol. Then, 10 μL of this suspension was dropped onto a glassy carbon electrode with a diameter of 5 mm and allowed to dry at room temperature. Linear sweep voltammetry (LSV) curves were measured in $O_2$-saturated phosphate buffer solution (0.1 M, pH = 6.86) with a scan rate of 0.005 V/s.

Photocurrent responses, electrochemical impedance spectroscopy (EIS), and Mott-Schottky plots measurements were conducted with a standard three-electrode system in $Na_2SO_4$ solution (0.5 M) on the CHI 760E electrochemical workstation. A platinum wire and an Ag/AgCl electrode were used as the counter electrode and reference electrode, respectively. A fluoride tin oxide (FTO) electrode loaded with sample was used as the working electrode. The fabrication of the working electrode was achieved by dropping the photocatalyst dispersion onto the FTO substrate with a similar thickness and dried in air.

### 2.8. Theoretical calculation

The calculations involving geometry optimization and the determination of Gibbs free energy during the oxygen reduction process were conducted using the Vienna Ab-initio Simulation Package (VASP) [28–30]. The interaction between the atomic cores with electrons was addressed using a projector augmented wave (PAW) pseudopotential. And the energy cutoff for this pseudopotential was set as 500 eV. In addition, the exchange-correlation function was modeled with the Perdew-Burke-Ernzerhof (PBE) method, which fall under the generalized gradient approximation (GGA) frameworks. The convergence accuracy for the force of each atom is set to within 0.02 eV/Å. The vacuum layer was set to 20 Å to eliminate the influence. Brillouin zone integration was conducted on a Γ-centered Monkhorst-Pack k-point mesh.

## 3. Results and discussion

### 3.1. Synthesis and characterization of the catalyst

Fig. 1a gives the schematic cartoon illustrating the synthesis of CDs decorated $Zn_{0.5}Cd_{0.5}S$. Initially, CDs with an average diameter of 2.2 nm were prepared by electrochemically anodic oxidation of alcohol (Fig. 1b, S2). HRTEM image shows a lattice distance of 0.21 nm, corresponding to the (100) crystal plane of carbon dots [31]. Then, CDs was in-situ loaded on $Zn_{0.5}Cd_{0.5}S$ through the formation of interfacial amide bonds during the hydrothermal process. As shown in Fig. S3, CDs decorated $Zn_{0.5}Cd_{0.5}S$ and control samples exhibit main peaks corresponding to hexagonal $Zn_{0.5}Cd_{0.5}S$ (JCPDS No. 89–2943). Owing to the low content and low crystallinity of CDs, no characteristic peaks of CDs can be observed (Figs. S3, S4). SEM images of $ZCS_{1EDA\text{-}10CDs}$, $ZCS_{1EDA}$, and

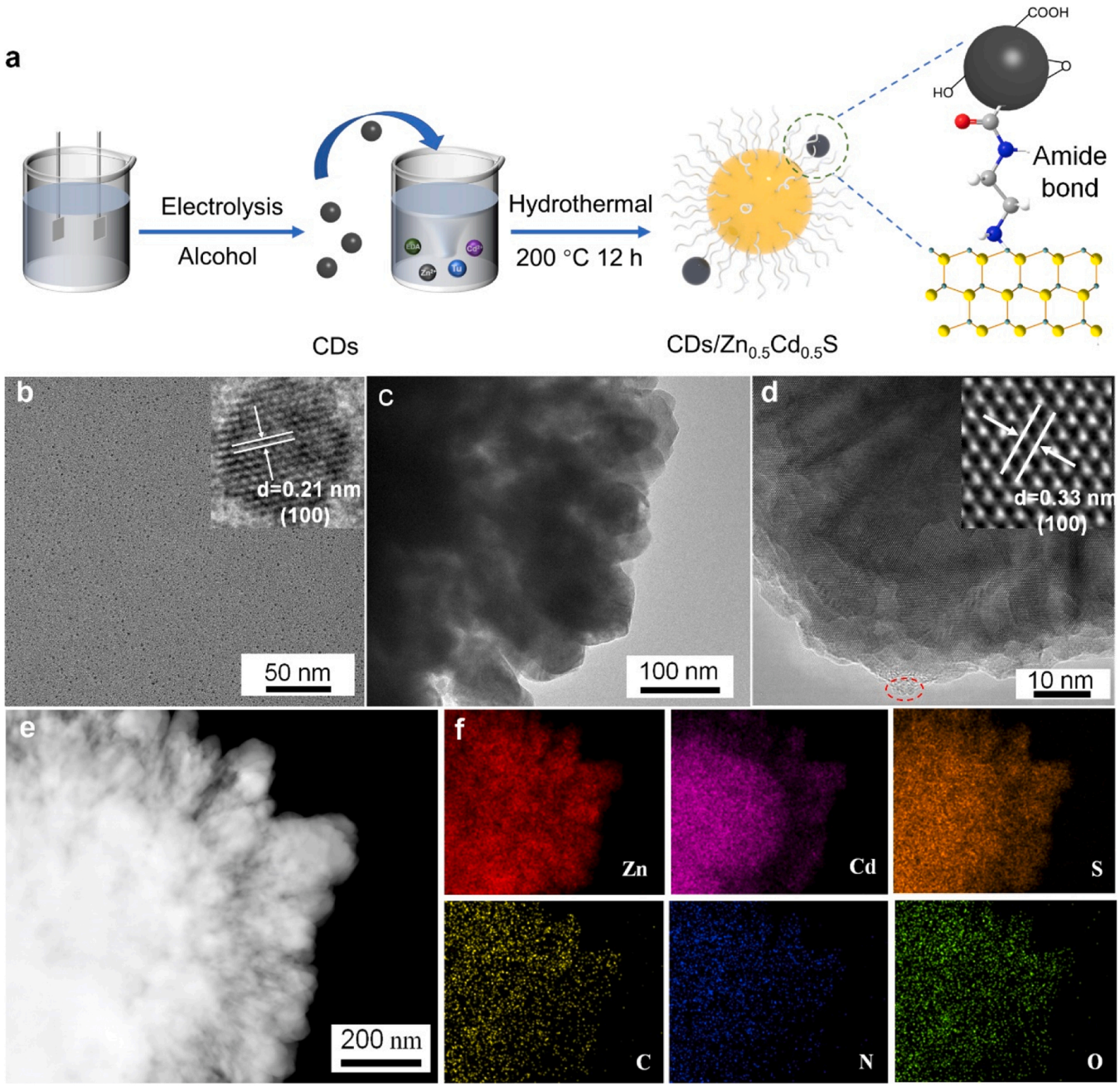


**Fig. 1.** (a) Schematic illustration for the synthesis of $ZCS_{1EDA\text{-}10CDs}$. (b) TEM image of CDs (The inset shows the HRTEM image). (c-e) TEM, HRTEM, and HADDF-STEM images of $ZCS_{1EDA\text{-}10CDs}$. (f) EDS elemental mapping of $ZCS_{1EDA\text{-}10CDs}$.

$ZCS_{H2O}$ reveal the aggregation of nanoparticles, while $ZCS_{10CDs}$ presents a honeycomb microstructure (Fig. S5). Fig. 1c-e present TEM, HRTEM, and HADDF-STEM images of $ZCS_{1EDA\text{-}10CDs}$. The HRTEM image of $ZCS_{1EDA\text{-}10CDs}$ show a lattice distance of 0.33 nm, which is attributed to the (002) plane of $Zn_{0.5}Cd_{0.5}S$ (Fig. 1d) [20]. Additionally, amorphous carbon dot highlighted with red dashed line is observed at the edge of $Zn_{0.5}Cd_{0.5}S$. The EDS elemental mapping analysis of $ZCS_{1EDA\text{-}10CDs}$ demonstrates the uniform distribution of Zn, Cd, S, and C, N, O elements, indicating the successful loading of CDs on ZCS. (Fig. 1f).

FTIR and XPS were conducted to analyze surficial functional groups. In Fig. 2a, the FTIR spectrum of CDs exhibit characteristic peaks at 3450, 1640, 1600, 1385, 1350, and 1135 $cm^{-1}$, corresponding to the vibration of O–H, C═O, C═C, –COO, C–H, and C–O–C bond, respectively [32]. Compared to CDs, a weak peak located at 1150 $cm^{-1}$ is observed, indicating the formation of amide bond [33]. However, due to the low surface content of ethylenediamine and CDs, the intensity is very weak. To further confirm the presence of amide bond, CDs-EDA sample was synthesized from the reaction between CDs and EDA, which exhibits a rather prominent signal. In Fig. 2b, the high-resolution C 1 s XPS spectra of CDs and $ZCS_{10CDs}$ can be deconvoluted into three peaks related to C–C (284.8 eV), C–O (286.3 eV), and C═O (287.8 eV), indicating the presence of –COOH and –OH groups [34]. For $ZCS_{1EDA\text{-}10CDs}$ and CDs-EDA, the peaks corresponding to C–O and C═O shift to a lower binding energy region. Additionally, a new peak at 285.6 eV appears, which can be assigned to the C–N bond. The high-resolution N 1 s spectrum (Fig. 2c) of $ZCS_{1EDA}$ shows a weak peak at 399.5 eV, corresponding to the primary amine ($–NH_2$) group. For $ZCS_{1EDA\text{-}10CDs}$, and CDs-EDA, the peak at 401.4 eV can be assigned to the amide bond [34]. This indicates that CDs are chemically adsorbed on ZCS via interfacial amide bond. The O 1 s spectra of CDs and $ZCS_{10CDs}$ display two peaks at 531.4 eV (C–O) and 532.5 eV (C═O), respectively (Fig. 2c) [24]. For $ZCS_{1EDA\text{-}10CDs}$ and CDs-EDA, these two peaks shift to the low binding energy direction. The high-resolution XPS spectra of Zn 2p, Cd 3d, and S 2p in the $ZCS_{1EDA\text{-}10CDs}$ move to a high energy region (Fig. S6). The shift is attributed to the interaction between ZCS adsorbed with ethylenediamine and CDs, leading to electrons transfer from ZCS towards CDs.

The light harvesting capability was investigated by UV–vis absorption spectra. As supplied in Fig. S7, $ZCS_{1EDA\text{-}10CDs}$ shows a wide visible light absorption with a bandgap of 2.43 eV. The loading of CDs resulted in enhanced light absorption owing to the wide visible light absorption of CDs. The determination of the flat potential for $ZCS_{1EDA}$ and CDs (−0.55 V and −0.41 V) was achieved through Mott-Schottky plots. According to the n-type semiconductor feature, the conduction band potential of $ZCS_{1EDA}$ and CDs can be determined to be −0.75 eV and −0.61 eV, respectively. Fig. S8 demonstrates a suitable band alignment between ZCS and CDs, allowing for the smooth transfer of photoinduced electrons from $ZCS_{1EDA}$ to CDs. The wettability of catalysts also plays an important role in the performance [35]. As revealed in Fig. S9, a smaller contact angle of 18° for $ZCS_{1EDA\text{-}10CDs}$ indicates better hydrophilicity. Firstly, we investigated the effect of EDA and Tu content on the photocatalytic performance. Fig. 3a and Fig. S10 show that the photocatalytic activity was significantly enhanced with the increase of EDA and Tu.

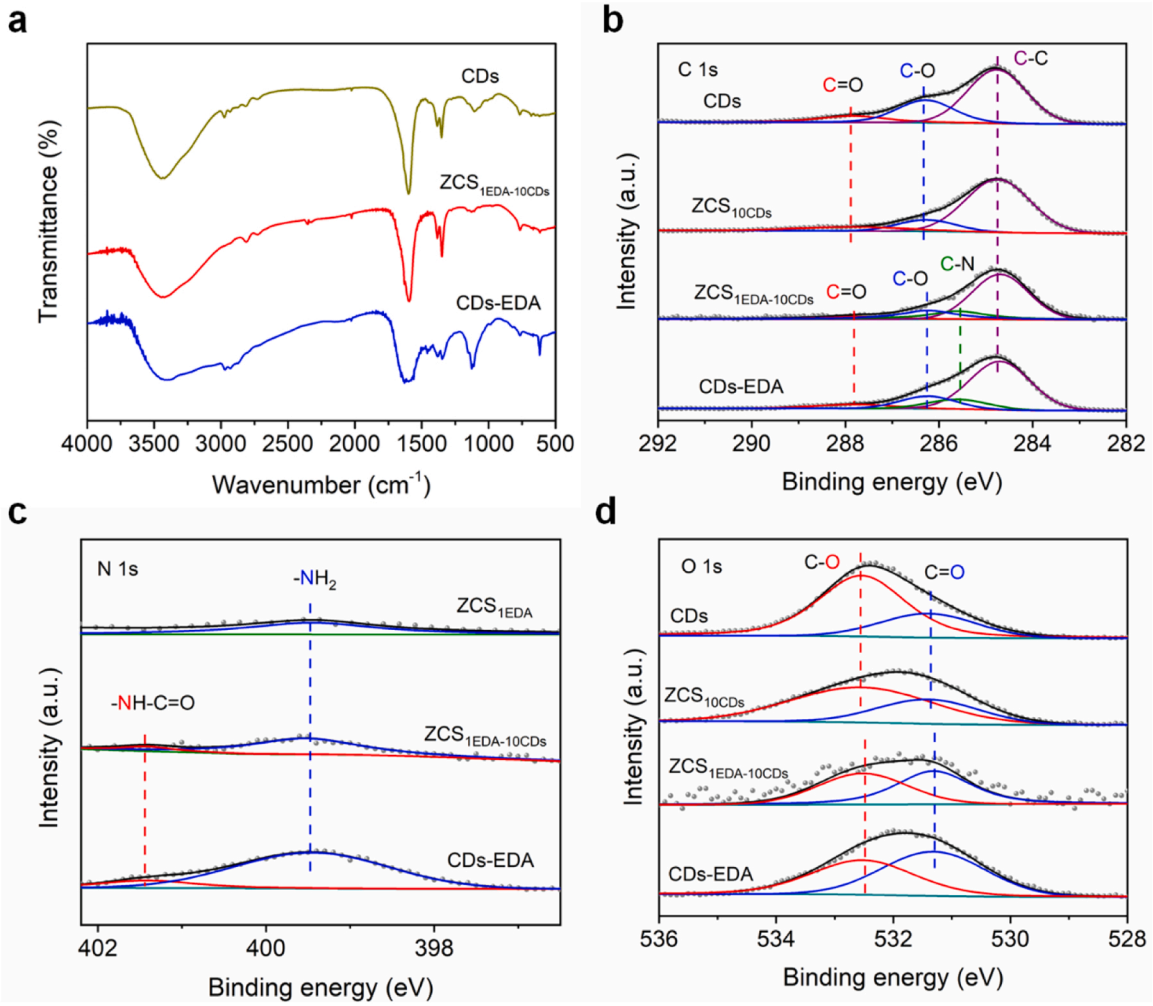


**Fig. 2.** (a) FTIR spectra of CDs, CDs-EDA, and $ZCS_{1EDA\text{-}10CDs}$. (b) High-resolution C 1 s spectra of CDs, $ZCS_{10CDs}$, $ZCS_{1EDA\text{-}10CDs}$ and CDs-EDA. (c) High-resolution N 1 s spectra of $ZCS_{1EDA}$, $ZCS_{1EDA\text{-}10CDs}$, and CDs-EDA. (d) High-resolution O 1 s spectra of CDs, $ZCS_{10CDs}$, $ZCS_{1EDA\text{-}10CDs}$, and CDs-EDA.

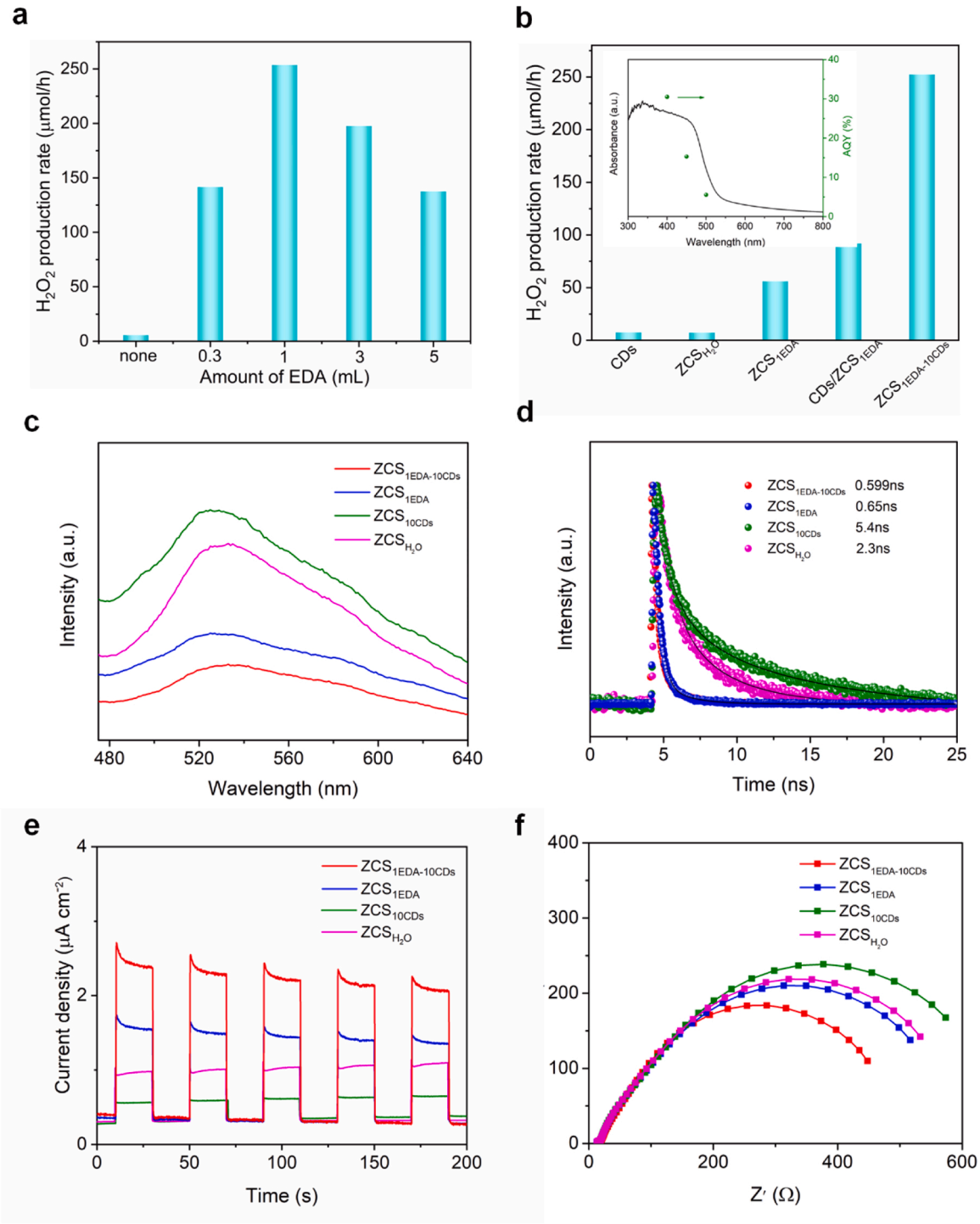


**Fig. 3.** (a) Photocatalytic $H_2O_2$ production performance of $ZCS_{xEDA-10CDs}$. (b) Comparison of photocatalytic $H_2O_2$ production rate of $ZCS_{1EDA-10CDs}$ with control samples. The inset is wavelength dependence AQY of photocatalytic $H_2O_2$ production over $ZCS_{1EDA-10CDs}$. (c) Steady PL, (d) time-resolved PL decay spectra, (e) transient photocurrent responses, and (f) EIS Nyquist plots of $ZCS_{1EDA-10CDs}$, $ZCS_{1EDA}$, $ZCS_{10CDs}$, $ZCS_{H2O}$.

When the amount of EDA and concentration of Tu reaches 1 mL and 1.6 M, a remarkable photocatalytic $H_2O_2$ production rate of 252 μmol/h is achieved, surpassing that of most reported photocatalysts (Table S1). The AQY at 400 nm is as high as 31 %. Furthermore, the $H_2O_2$ yield exhibits an approximately linear increase during the 5 h test (Fig. S11). The SEM image, XRD patterns, and XPS spectra of the recovered catalyst show no obvious change, demonstrating its good stability (Fig. S12). To identify the key factors affecting photocatalytic performance, a series of control experiments were conducted. As described in Fig. 3b, the $H_2O_2$ production rate of $ZCS_{1EDA-10CDs}$ is 42, 34, and 4.5 times of that of $ZCS_{10CDs}$, $ZCS_{H2O}$, and $ZCS_{1EDA}$, respectively, highlighting the significant role of EDA and CDs in enhancing the photocatalytic performance. In addition, $CDs/ZCS_{1EDA}$ obtained by physically adsorbing CDs onto $ZCS_{1EDA}$ exhibits a production rate of 90 μmol/h, which is higher than $ZCS_{1EDA}$ but much lower than that of $ZCS_{1EDA-10CDs}$. To further clarify the impact of interfacial amide bond on the performance, $ZCS_{1EDA-10CDs}$ was subjected to calcination at 300 °C under Ar atmosphere to break the amide bond bridge. Following the calcination, a significant decrease in

the photocatalytic $H_2O_2$ production rate was observed, dropping from 252 μmol/h to 160 μmol/h (Fig. S13). These results confirm that the CDs are beneficial for the $H_2O_2$ production. Moreover, the interfacial amide bond between ZCS and CDs is responsible for the excellent performance. A series of active species trapping experiments were conducted to elucidate the photosynthesis mechanism of $H_2O_2$ over $ZCS_{1EDA\text{-}10CDs}$ (Fig. S14). The control experiments demonstrate that catalyst, light and oxygen are indispensable for the generation of $H_2O_2$. These results reveal that photocatalytic $H_2O_2$ production is a light-driven oxygen reduction process. Moreover, $H_2O_2$ yield is seriously inhibited after the introduction of p-benzoquinone (pBQ) as a scavenger for superoxide anion radical, demonstrating that two-step single electron transfer is the primary route for $H_2O_2$ generation. The separation of photoinduced electrons and holes was studied by PL and photoelectrochemical tests. Fig. 3c shows that $ZCS_{1EDA\text{-}10CDs}$ exhibits the lowest PL intensity, indicating fast separation of photogenerated charge carriers. Time-resolved PL analysis reveals that the average lifetime of excited $ZCS_{1EDA\text{-}10CDs}$ (0.599 ns) is shorter than that of $ZCS_{1EDA}$ (0.65 ns), $ZCS_{10CDs}$ (5.4 ns) and $ZCS_{H2O}$ (2.3 ns). This suggests a prompt transfer of photoinduced electron from ZCS to CDs through the electron transfer bridge (amide bond) (Fig. 3d and Table S2) [36]. An enhanced photocurrent and a smaller diameter of semicircles in the EIS test over $ZCS_{1EDA\text{-}10CDs}$ imply its higher mobility of photoinduced electrons with lower charge-transfer resistance (Fig. 3e, f).

To further investigate the transfer process of photogenerated electrons, XPS characterization under dark and light illumination was conducted. Fig. 4 illustrates that the XPS peaks of Cd 3d, Zn 2p and S 2p of $ZCS_{1EDA\text{-}10CDs}$ display a red shift to high binding energy region, while the C 1 s signal shifts to a lower binding energy region upon light illumination. These observations indicate that photo-induced electrons are transferred from ZCS to CDs [37]. The interfacial amide bond acts as a high-speed electron transfer channel, facilitating the separation of photogenerated electrons and holes.

Superoxide anion radical ($\bullet O_2^-$) is a crucial intermediate in the indirect oxygen reduction pathway leading to the formation of $H_2O_2$. EPR with DMPO as the spin-trapping reagent was employed to probe the formation of $\bullet O_2^-$ radicals [38–40]. Fig. 5a reveals that no apparent signal occurs over $ZCS_{10CDs}$ and $ZCS_{H2O}$, while an enhanced signal appears over $ZCS_{1EDA}$. Notably, $ZCS_{1EDA\text{-}10CD}$ exhibit a more prominent DMPO-$\bullet O_2^-$signal, indicating the formation of high concentration of $\bullet O_2^-$. The improved $\bullet O_2^-$ production capability of $ZCS_{1EDA\text{-}10CDs}$ is ascribed to the efficient transfer of photoinduced electrons from ZCS to CDs. Furthermore, CDs with abundant oxygenous functional groups serve as active sites to accelerate the ORR rate. To study the selectivity of oxygen reduction, rotating disk electrode (RDE) test was performed. The linear sweep voltammograms (LSV) of $ZCS_{1EDA}$, $ZCS_{10CDs}$, $ZCS_{H2O}$, and $ZCS_{1EDA\text{-}10CDs}$ under different rotational speeds were obtained (Fig. S15) Fig. 5b shows the electron transfer numbers calculated through the fitting of Koutecky-Levich curve. The electron transfer numbers of $ZCS_{10CDs}$, $ZCS_{H2O}$, and $ZCS_{1EDA}$ are 1.34, 1.39, and 1.67, respectively. In contrast, the electrons transfer number for $ZCS_{1EDA\text{-}10CDs}$ (2.06) is very close to 2, demonstrating its high selectivity of $2e^-$ ORR [41–45]. To gain

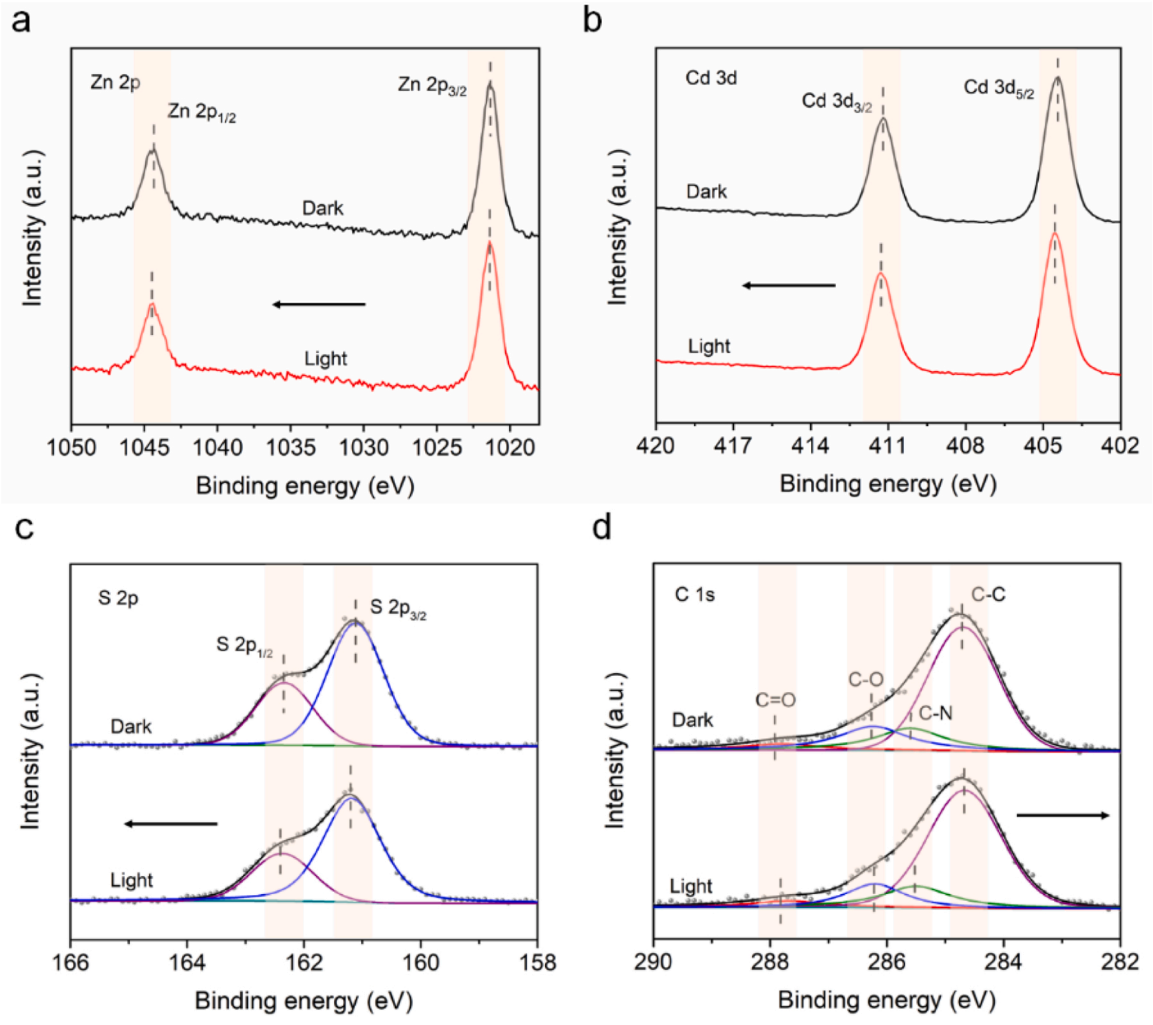


**Fig. 4.** XPS spectra of $ZCS_{1EDA\text{-}10CDs}$ in darkness and under light irradiation for (a) Zn 2p, (b) Cd 3d, (c) S 2p and (d) C 1 s.

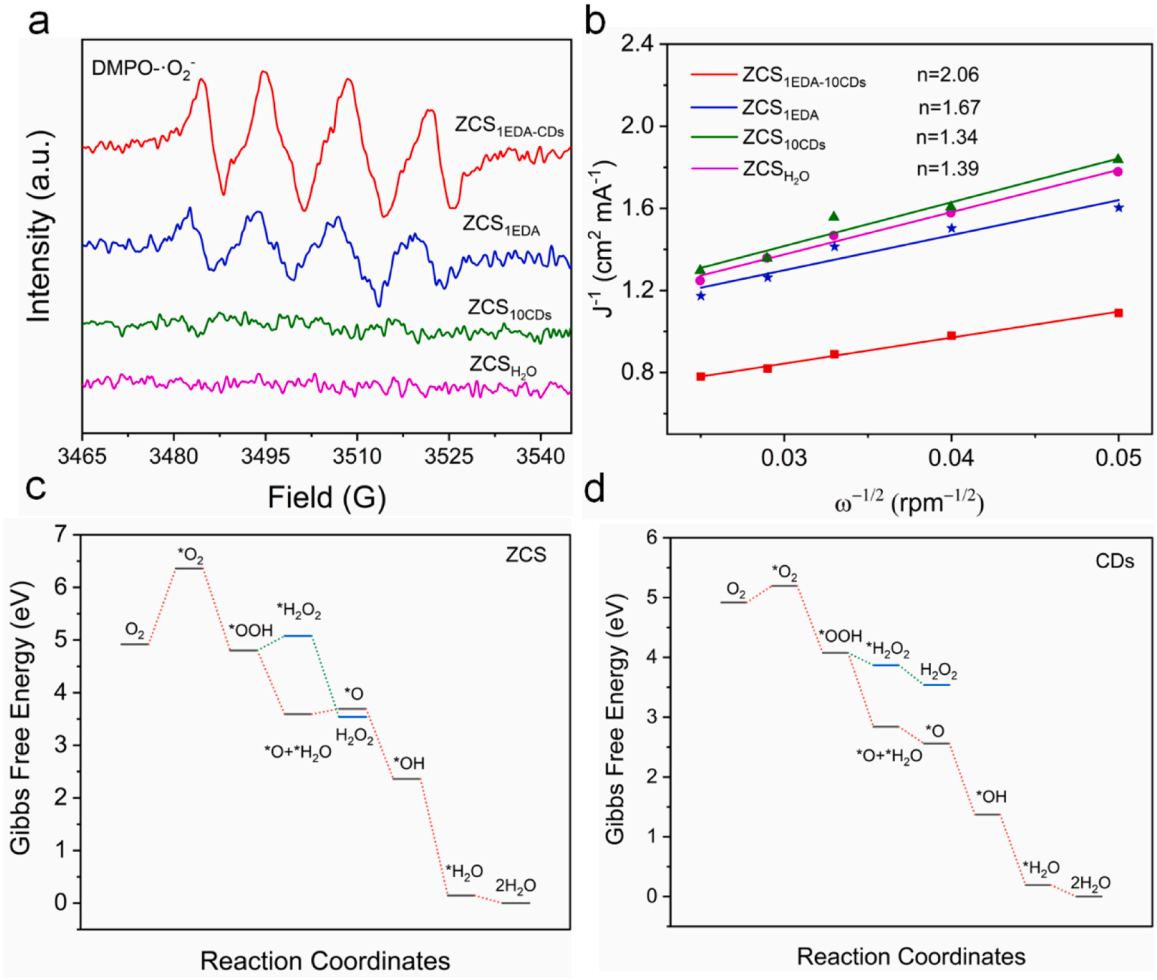


**Fig. 5.** (a) EPR signal of DMPO-•$O_2^-$ over $ZCS_{1EDA\text{-}10CDs}$, $ZCS_{1EDA}$, $ZCS_{10CDs}$, $ZCS_{H2O}$ under visible light. (b) Koutecky-Levich plots (at −0.799 V vs. Ag/AgCl). (c, d) Gibbs free energy diagram of two- and four-electron ORR pathways over ZCS and CDs.

further understanding of the role of CDs during the ORR, DFT calculations were conducted. The optimized models of ZCS and CDs (Figs. S16, 17) were used to simulate the Gibbs free energy of ORR from the thermodynamic perspective [46]. Compared to ZCS (1.44 eV), CDs show a significantly lower free energy (0.28 eV) for $O_2$ adsorption, suggesting favorable $O_2$ adsorption and activation on the surface of CDs. Moreover, a lower free energy (−0.21 eV) is achieved for CDs than that of ZCS (0.28 eV) to accomplish the transformation from *OOH to $H_2O_2$, proving an improved $2e^-$ oxygen reduction selectivity towards $H_2O_2$. All in all, efficient photogenerated electrons transfer from ZCS to CDs has been achieved through the high-speed electron bridge (amide bond) under visible light illumination. Furthermore, CDs with ample oxygenous groups serve as active sites, enabling highly efficient and selective $2e^-$ oxygen reduction to $H_2O_2$.

## 4. Conclusions

In summary, carbon dots decorated $Zn_{0.5}Cd_{0.5}S$ bridged with interfacial amide bond was successfully fabricated by a simple hydrothermal method. The formation of intimate contact between carbon dots and $Zn_{0.5}Cd_{0.5}S$ not only improves the wettability, but also accelerates the separation of photoinduced electrons from $Zn_{0.5}Cd_{0.5}S$ to carbon dots. Moreover, carbon dots with rich oxygenous functional groups serve as active centers for oxygen reduction, improving oxygen reduction rate and the selectivity of $2e^-$ reduction towards $H_2O_2$. Thus, a 34-fold enhancement in photocatalytic $H_2O_2$ production performance is achieved over $ZCS_{1EDA\text{-}10CDs}$ with a generation rate of 252 μmol/h and an AQY at 400 nm as high as 31 %. This work provides a rational design concept for highly efficient photocatalysts for $H_2O_2$ production via the $O_2$ reduction route. Moreover, the novel insight gained from the utilization of interfacial chemical bonds as high-speed electron transfer channels opens up new opportunities for the design of other advanced materials.

## CRediT authorship contribution statement

**Yao Shuang:** Writing – review & editing. **Yang Fan:** Writing – review & editing, Supervision. **An Changhua:** Writing – review & editing, Supervision, Conceptualization. **Tang Ting:** Writing – original draft, Visualization. **Shen Yongli:** Writing – original draft. **Zhao Jiwu:** Writing – review & editing, Formal analysis.

## Declaration of Competing Interest

The authors declare that they have no known competing financial interests or personal relationships that could have appeared to influence the work reported in this paper.

## Data availability

Data will be made available on request.

## Acknowledgments

The authors acknowledge the financial support of Natural Science Foundation of China (22275139, 21971190), Key Project of Natural Science Foundation of Tianjin City (Contract No. 22JCZDJC00510), Natural Science Foundation of Tianjin (20JCQNJC00520), and China Scholarship Council.

## Appendix A. Supporting information

Supplementary data associated with this article can be found in the online version at doi:10.1016/j.apcatb.2024.123721.

## References

[1] Y. Zhang, C. Pan, G. Bian, J. Xu, Y. Dong, Y. Zhang, Y. Lou, W. Liu, Y. Zhu, $H_2O_2$ generation from $O_2$ and $H_2O$ on a near-infrared absorbing porphyrin supramolecular photocatalyst, Nat. Energy 8 (2023) 361–371.
[2] H. Tan, P. Zhou, M. Liu, Q. Zhang, F. Liu, H. Guo, Y. Zhou, Y. Chen, L. Zeng, L. Gu, Z. Zheng, M. Tong, S. Guo, Photocatalysis of water into hydrogen peroxide over an atomic Ga-N5 site, Nat. Synth. 2 (2023) 557–563.
[3] Y. Xia, X. Zhao, C. Xia, Z.-Y. Wu, P. Zhu, J.Y. Kim, X. Bai, G. Gao, Y. Hu, J. Zhong, Y. Liu, H. Wang, Highly active and selective oxygen reduction to $H_2O_2$ on boron-doped carbon for high production rates, Nat. Commun. 12 (2021) 4225.
[4] P. Sun, Z. Chen, J. Zhang, G. Wu, Y. Song, Z. Miao, K. Zhong, L. Huang, Z. Mo, H. Xu, Simultaneously tuning electronic reaction pathway and photoactivity of P, O modified cyano-rich carbon nitride enhances the photosynthesis of $H_2O_2$, Appl. Catal. B 342 (2024) 123337.
[5] Q. You, C. Zhang, M. Cao, B. Wang, J. Huang, Y. Wang, S. Deng, G. Yu, Defects controlling, elements doping, and crystallinity improving triple-strategy modified carbon nitride for efficient photocatalytic diclofenac degradation and $H_2O_2$ production, Appl. Catal. B 321 (2023) 121941.
[6] E. Jung, H. Shin, B.-H. Lee, V. Efremov, S. Lee, H.S. Lee, J. Kim, W. Hooch Antink, S. Park, K.-S. Lee, S.-P. Cho, J.S. Yoo, Y.-E. Sung, T. Hyeon, Atomic-level tuning of Co–N–C catalyst for high-performance electrochemical $H_2O_2$ production, Nat. Mater. 19 (2020) 436–442.
[7] Q. Zhang, X. Tan, N.M. Bedford, Z. Han, L. Thomsen, S. Smith, R. Amal, X. Lu, Direct insights into the role of epoxy groups on cobalt sites for acidic $H_2O_2$ production, Nat. Commun. 11 (2020) 4181.
[8] C. Yang, S. Wan, B. Zhu, J. Yu, S. Cao, Calcination-regulated microstructures of donor-acceptor polymers towards enhanced and stable photocatalytic $H_2O_2$ production in pure water, Angew. Chem. Int. Ed. 134 (2022) e202208438.
[9] H. Che, X. Gao, J. Chen, J. Hou, Y. Ao, P. Wang, Iodide-induced fragmentation of polymerized hydrophilic carbon nitride for high-performance quasi-homogeneous photocatalytic $H_2O_2$ production, Angew. Chem. Int. Ed. 60 (2021) 25546–25550.
[10] J.S. Lim, J.H. Kim, J. Woo, D.San Baek, K. Ihm, T.J. Shin, Y.J. Sa, S.H. Joo, Designing highly active nanoporous carbon $H_2O_2$ production electrocatalysts through active site identification, Chem 7 (2021) 3114–3130.
[11] H. Wang, C. Yang, F. Chen, G. Zheng, Q. Han, A crystalline partially fluorinated triazine covalent organic framework for efficient photosynthesis of hydrogen peroxide, Angew. Chem. Int. Ed. 61 (2022) e202202328.
[12] C. Feng, L. Tang, Y. Deng, J. Wang, J. Luo, Y. Liu, X. Ouyang, H. Yang, J. Yu, J. Wang, Synthesis of leaf-vein-Like g-$C_3N_4$ with tunable band structures and charge transfer properties for selective photocatalytic $H_2O_2$ evolution, Adv. Funct. Mater. 30 (2020) 2001922.
[13] J. Tang, T. Zhao, D. Solanki, X. Miao, W. Zhou, S. Hu, Selective hydrogen peroxide conversion tailored by surface, interface, and device engineering, Joule 5 (2021) 1432–1461.
[14] M. Kou, Y. Wang, Y. Xu, L. Ye, Y. Huang, B. Jia, H. Li, J. Ren, Y. Deng, J. Chen, Molecularly engineered covalent organic frameworks for hydrogen peroxide photosynthesis, Angew. Chem. Int. Ed. 61 (2022) e202200413.
[15] W. Yu, C. Hu, L. Bai, N. Tian, Y. Zhang, H. Huang, Photocatalytic hydrogen peroxide evolution: What is the most effective strategy? Nano Energy 104 (2022) 107906.
[16] Y. Zheng, Y. Luo, Q. Ruan, S. Wang, J. Yu, X. Guo, W. Zhang, H. Xie, Z. Zhang, Y. Huang, Plasma-induced hierarchical amorphous carbon nitride nanostructure with two $N_2$ C-site vacancies for photocatalytic $H_2O_2$ production, Appl. Catal. B 311 (2022) 121372.
[17] Y. Yang, J. Liu, M. Gu, B. Cheng, L. Wang, J. Yu, Bifunctional $TiO_2$/COF S-scheme photocatalyst with enhanced $H_2O_2$ production and furoic acid synthesis mechanism, Appl. Catal. B 333 (2023) 122780.
[18] L. Ning, X. Chen, Z. Wang, J. Xu, High-efficiency pollutant degradation, disinfection and $H_2O_2$ production activities of magnetically separable Co-imbedded N-doped carbonaceous framework/supramolecular perylene diimide photocatalyst, Appl. Catal. B 324 (2023) 122282.
[19] W. Huang, C. Su, C. Zhu, T. Bo, S. Zuo, W. Zhou, Y. Ren, Y. Zhang, J. Zhang, M. Rueping, Isolated electron trap-induced charge accumulation for efficient photocatalytic hydrogen production, Angew. Chem. Int. Ed. (2023) e202304634.
[20] Z. Li, W. Zhou, Y. Tang, X. Tan, Y. Zhang, Z. Geng, Y. Guo, L. Liu, T. Yu, J. Ye, Insights into the operation of noble-metal-free cocatalyst 1T-$WS_2$-decorated $Zn_{0.5}Cd_{0.5}S$ for enhanced photocatalytic hydrogen evolution, ChemSusChem 14 (2021) 4752–4763.
[21] F. Yang, S. Liu, T. Tang, S. Yao, C. An, Visible-light driven $H_2$ evolution coupled with furfuryl alcohol selective oxidation over Ru atom decorated $Zn_{0.5}Cd_{0.5}S$ nanorods, Catal. Sci. Technol. 13 (2023) 2469–2474.
[22] Y. Zhao, L. Xu, X. Wang, Z. Wang, Y. Liu, Y. Wang, Q. Wang, Z. Wang, H. Huang, Y. Liu, W.-Y. Wong, Z. Kang, A comprehensive understanding on the roles of carbon dots in metallated graphyne based catalyst for photoinduced $H_2O_2$ production, Nano Today 43 (2022) 101428.
[23] M. Gu, D.-Y. Lee, J. Mun, D. Kim, H.-i Cho, B. Kim, W. Kim, G. Lee, B.-S. Kim, H.-i Kim, Solar-to-hydrogen peroxide conversion of photocatalytic carbon dots with anthraquinone: Unveiling the dual role of surface functionalities, Appl. Catal. B 312 (2022) 121379.
[24] Y. Guo, R. Zhang, S. Zhang, H. Hong, Y. Zhao, Z. Huang, C. Han, H. Li, C. Zhi, Ultrahigh oxygen-doped carbon quantum dots for highly efficient $H_2O_2$ production via two-electron electrochemical oxygen reduction, Energy Environ. Sci. 15 (2022) 4167–4174.
[25] G. Wei, K. Du, X. Zhao, Z. Wang, M. Liu, C. Li, H. Wang, C. An, W. Xing, Carbon quantum dot-induced self-assembly of ultrathin $Ni(OH)_2$ nanosheets: a facile method for fabricating three-dimensional porous hierarchical composite micro-nanostructures with excellent supercapacitor performance, Nano Res. 10 (2017) 3005–3017.
[26] C. An, J. Feng, J. Liu, G. Wei, J. Du, H. Wang, S. Jin, J. Zhang, NiS nanoparticle decorated $MoS_2$ nanosheets as efficient promoters for enhanced solar $H_2$ evolution over $ZnxCd_{1-x}S$ nanorods, Inorg. Chem. Front. 4 (2017) 1042–1047.
[27] S. Yao, T. Tang, Y. Shen, F. Yang, C. An, Atomically dispersed scandium Lewis acid sites on carbon nitride for efficient photocatalytic hydrogen peroxide production, Sci. China Mater. 66 (2023) 672–678.
[28] G. Kresse, J. Furthmüller, Efficiency of ab-initio total energy calculations for metals and semiconductors using a plane-wave basis set, Comput. Mater. Sci. 6 (1996) 15–50.
[29] G. Kresse, J. Furthmüller, Efficient iterative schemes for ab initio total-energy calculations using a plane-wave basis set, Phys. Rev. B 54 (1996) 11169.
[30] P.E. Blöchl, Projector augmented-wave method, Phys. Rev. B 50 (1994) 17953.
[31] Y. Yu, Y. Feng, F. Liu, H. Wang, H. Yu, K. Dai, G. Zheng, W. Feng, Carbon dots-based ultrastretchable and conductive hydrogels for high-performance tactile sensors and self-powered electronic skin, Small 19 (2023) 2204365.
[32] J. Deng, Q. Lu, N. Mi, H. Li, M. Liu, M. Xu, L. Tan, Q. Xie, Y. Zhang, S. Yao, Electrochemical synthesis of carbon nanodots directly from alcohols, Chem. Eur. J. 20 (2014) 4993–4999.
[33] K. Anastasiadis, G. Eliades, 8 8-Dentine conditioners: effect on collagen probed by amide-III peak analysis, Dent. Mater. 38 (2022) e5.
[34] K. Wei, H. Nie, Y. Li, X. Wang, Y. Liu, Y. Zhao, H. Shi, H. Huang, Y. Liu, Z. Kang, Carbon dots with different energy levels regulate the activity of metal-free catalyst for hydrogen peroxide photoproduction, J. Colloid Interface Sci. 616 (2022) 769–780.
[35] J. Du, Y. Shen, F. Yang, J. Wei, K. Xu, X. Li, C. An, In-situ topology synthesis of defective MoN nanosheets/g-$C_3N_4$ 2D/2D heterojunction photocatalyst for efficient $H_2$ production, Appl. Surf. Sci. 608 (2023) 155199.
[36] F. Yang, D. Liu, Y. Li, L. Cheng, J. Ye, Salt-template-assisted construction of honeycomb-like structured g-$C_3N_4$ with tunable band structure for enhanced photocatalytic $H_2$ production, Appl. Catal. B 240 (2019) 64–71.
[37] S. Tao, W. Zhong, Y. Chen, F. Chen, P. Wang, H. Yu, Bifunctional thioacetamide-mediated synthesis of few-layered $MoOS_x$ nanosheet-modified CdS hollow spheres for efficient photocatalytic $H_2$ production, Catal. Sci. Technol. 12 (2022) 6006–6015.
[38] Z. Luo, X. Chen, Y. Hu, X. Chen, W. Lin, X. Wu, X. Wang, Side-chain molecular engineering of triazole-based donor-acceptor polymeric photocatalysts with strong electron push-pull interactions, Angew. Chem. Int. Ed. (2023) e202304875.
[39] P. Ren, T. Zhang, N. Jain, H.V. Ching, A. Jaworski, G. Barcaro, S. Monti, J. Silvestre-Albero, V. Celorrio, L. Chouhan, An atomically dispersed Mn-photocatalyst for generating hydrogen peroxide from seawater via the water oxidation reaction (WOR, ), J. Am. Chem. Soc. 145 (2023) 16584–16596.
[40] W. Wang, Q. Song, Q. Luo, L. Li, X. Huo, S. Chen, J. Li, Y. Li, S. Shi, Y. Yuan, Photothermal-enabled single-atom catalysts for high-efficiency hydrogen peroxide photosynthesis from natural seawater, Nat. Commun. 14 (2023) 2493.
[41] X. Zhao, Y. You, S. Huang, Y. Wu, Y. Ma, G. Zhang, Z. Zhang, Z-scheme photocatalytic production of hydrogen peroxide over $Bi_4O_5Br_2$/g-$C_3N_4$ heterostructure under visible light, Appl. Catal. B 278 (2020) 119251.
[42] X. Li, S. Yang, M. Liu, X. Yang, Q. Xu, G. Zeng, Z. Jiang, Catalytic linkage engineering of covalent organic frameworks for the oxygen reduction reaction, Angew. Chem. Int. Ed. (2023) e202304356.
[43] X. Wang, X. Yang, C. Zhao, Y. Pi, X. Li, Z. Jia, S. Zhou, J. Zhao, L. Wu, J. Liu, Ambient preparation of benzoxazine-based phenolic resins enables long-term sustainable photosynthesis of hydrogen peroxide, Angew. Chem. Int. Ed. 135 (2023) e202302829.
[44] C. Yang, S. Wan, B. Zhu, J. Yu, S. Cao, Calcination-regulated microstructures of donor-acceptor polymers towards enhanced and stable photocatalytic $H_2O_2$ production in pure water, Angew. Chem. Int. Ed. 134 (2022) e202208438.
[45] C. Feng, Z.P. Wu, K.W. Huang, J. Ye, H. Zhang, Surface modification of 2D photocatalysts for solar energy conversion, Adv. Mater. 34 (2022) 2200180.
[46] Y. Li, Y. Guo, D. Luan, X. Gu, X.-W. Lou, An unlocked two-dimensional conductive Zn-MOF on polymeric carbon nitride for photocatalytic $H_2O_2$ production, Angew. Chem. Int. Ed. (2023) e202310847.